CHINESE OPTICS LETTERS

Vol. 21, No. 12 | December 2023

QAM signal with electric field sensor based on thin-film lithium niobate [Invited]

Tingan Li (李廷安)[1], Zhao Liu (刘 钊)[2], An Pan (潘 安)[1], Chenglin Shang (尚成林)[1], Yong Liu (刘 永)[2], Cheng Zeng (曾 成)[1*], and Jinsong Xia (夏金松)[1]

[1] Wuhan National Laboratory for Optoelectronics, Huazhong University of Science and Technology, Wuhan 430074, China

[2] School of Optoelectronic Science and Engineering, University of Electronic Science and Technology of China, Chengdu 610054, China

*Corresponding author: zengchengwuli@hust.edu.cn

Received August 31, 2023 | Accepted October 31, 2023 | Posted Online December 13, 2023

Large-bandwidth, high-sensitivity, and large dynamic range electric field sensors are gradually replacing their traditional counterparts. The lithium-niobate-on-insulator (LNOI) material has emerged as an ideal platform for developing such devices, owing to its low optical loss, high electro-optical modulation efficiency, and significant bandwidth potential. In this paper, we propose and demonstrate an electric field sensor based on LNOI. The sensor consists of an asymmetric Mach–Zehnder interferometer (MZI) and a tapered dipole antenna array. The measured fiber-to-fiber loss is less than −6.7 dB, while the MZI structure exhibits an extinction ratio of greater than 20 dB. Moreover, 64-QAM signals at 2 GHz were measured, showing an error vector magnitude (EVM) of less than 8%.

Keywords: thin-film lithium niobate; electric field sensor; QAM signal.
DOI: 10.3788/COL202321.120041

1. Introduction

With the continuous advancement of wireless technology, the proliferation of wireless devices is experiencing exponential growth[1,2]. Consequently, the electromagnetic environment in space is becoming increasingly complex. Electric field sensors play a crucial role in the assessment of the electromagnetic environment across a spectrum of applications, including atmospheric science, spacecraft and rocket launches, electromagnetic compatibility measurements, and long-term monitoring of high-voltage power lines[3–8]. These sensors are facing increasingly intricate usage scenarios. Therefore, there exists an urgent requirement for compact electric field sensors that offer low loss, large bandwidth coverage, and a large dynamic range.

Currently, traditional D-Dot electric field sensors can achieve bandwidths exceeding 10 GHz[9], while MEMS electric field sensors, as developed by Andreas Kainz and colleagues at Vienna University of Technology in 2018, have demonstrated dynamic ranges extending to 10^2–10^5 V/m[10]. Nonetheless, these sensors exhibit noteworthy limitations in their inability to simultaneously satisfy the requirements for large bandwidth and large dynamic range characteristics. Therefore, traditional electric field sensors are increasingly struggling to capture the complexities of electromagnetic environments adequately. Moreover, miniaturization and integration are identified as the future trends in this field. In the next generation of electric field sensor platforms, thin-film lithium niobate (TFLN) material emerges as a prominent candidate due to its excellent electro-optic effect, high integration capability, and low loss properties[11–15]. These advantages can also be applied to the development of electric field sensors, and devices with larger bandwidth, higher sensitivity, and a wider amplitude range have been fabricated in recent years[16–19]. Since 1993, researchers have been engaged in the exploration of wireless modulation using the lithium niobate platform in conjunction with antenna structures[20,21]. Subsequently, wireless modulator components rooted in the lithium niobate platform have been reported in succession, revealing robust performance and substantial potential in these aspects[22–26]. This indicates that LN materials exhibit good performance in electric field sensing and wireless transmission. As space electromagnetic signals become increasingly complex, sensors need to be capable of detecting various types of signals, rather than solely relying on bandwidth, dynamic range, or sensitivity assessments.

In previous work, we have tested a remarkable bandwidth of 26.5 GHz and a dynamic range spanning from 40 mV/m to 28.6 kV/m, utilizing electric field sensors fabricated on thin-film lithium niobate[27]. However, the device encountered slightly higher losses attributed to process limitations, resulting in fiber-to-fiber losses of approximately −20 dB. In this paper, by optimizing the device design and refining the fabrication process, we successfully mitigated the insertion loss of the

new device to approximately −6.7 dB. Moreover, we have measured quadrature amplitude modulation (QAM) signals using this device, which demonstrates the ability to recover information from the complex spatial electromagnetic field.

2. Device Design

The device primarily consists of a Mach–Zehnder interferometer (MZI) structure based on thin-film lithium niobate (LNOI) and a tapered dipole antenna. The utilization of the tapered dipole antenna is grounded in prior theoretical and experimental validations of its frequency-independent response[28], thereby enabling a larger bandwidth. The schematic depiction of its configuration is presented in Fig. 1(a) and is composed of two integral components: a conical antenna and a modulating electrode. The conical dipole antenna functions as a receptor for the spatial electric fields, subsequently facilitating the generation of an amplified electric field within the modulating electrode. Upon applying of an electric field to the waveguide, the orientation of the external electric field, not invariably aligned with the crystal spindle's direction, leads to a deformation of the ellipsoid equation as follows:

$$\left(\frac{1}{n^2}\right)_1 X^2 + \left(\frac{1}{n^2}\right)_2 Y^2 + \left(\frac{1}{n^2}\right)_3 Z^2 + 2\left(\frac{1}{n^2}\right)_4 XY + 2\left(\frac{1}{n^2}\right)_5 XZ + 2\left(\frac{1}{n^2}\right)_6 YZ = 1. \tag{1}$$

Here, X, Y, and Z symbolize the principal axes of the crystal, while n signifies the refractive index of the material. Furthermore, owing to the inherent linear electro-optical effect exhibited by the lithium niobate material, alterations in the crystal's refractive index demonstrate a direct linear correlation with the applied electric field. This relationship is encapsulated within the coefficient matrix denoted as γ, which finds its expression as follows:

$$\begin{bmatrix} \Delta\left(\frac{1}{n^2}\right)_1 \\ \Delta\left(\frac{1}{n^2}\right)_2 \\ \vdots \\ \Delta\left(\frac{1}{n^2}\right)_6 \end{bmatrix} = \begin{bmatrix} \gamma_{11} & \gamma_{12} & \gamma_{13} \\ \gamma_{21} & \gamma_{22} & \gamma_{23} \\ \vdots & \vdots & \vdots \\ \gamma_{61} & \gamma_{62} & \gamma_{63} \end{bmatrix} \cdot \begin{bmatrix} E_x \\ E_y \\ E_z \end{bmatrix}, \tag{2}$$

when using an X-cut thin-film lithium niobate crystal element in the design leads to the propagation of the lithium niobate waveguide along the Y-direction of the crystal. Consequently, the electric field aligns itself with the Z-axis direction of the lithium niobate crystal ($E_x = 0$, $E_y = 0$). At this time, when the electric field intensity applied between the electrodes on both sides of the arm can be properly modulated by the above two expressions, the refractive index of the extraordinary light changes by $n' \approx n - \frac{1}{2}n^3\gamma_{33}E_z$, and the phase difference of the light in the two arms of the MZI structure can be modulated by the change of the refractive index.

In this design, the antenna layer's height is 2 mm, as shown in Fig. 1(a); there are four groups of antennas placed on the same modulation arm. To avoid the potential mutual coupling, the lateral distance between these antennas is set to 1 mm. The simulation of the S_{11} curve of these antennas utilizing the HFSS software is shown in Fig. 1(b). The red curve represents the S_{11} of the single antenna, while the black curve represents the S_{11} of the four antennas used in the device. It can be observed that there is a flat response at 20 GHz, but there is still some difference between the two curves due to the mutual coupling effect between the antennas. When the gap between each antenna is increased, the two curves become more similar.

Figure 2(a) presents the electric field sensor structure. This sample is fabricated from an X-cut LNOI crystal, featuring the previously mentioned four sets of conical dipole antennas. Fiber coupling is achieved through the spot size converter (SSC), while 1×2 multi-mode interference (MMI) couplers handle the splitting and recombination of light. The multi-mode interference section measures 23.6 μm in length and 5.6 μm in width. Additionally, an asymmetric Mach–Zehnder interferometer (MZI) configuration is adopted, inducing an inherent phase difference between the two modulation arms which could be expressed by formula $\varphi = 2\pi \cdot \Delta L \cdot n/\lambda$. The ΔL represents

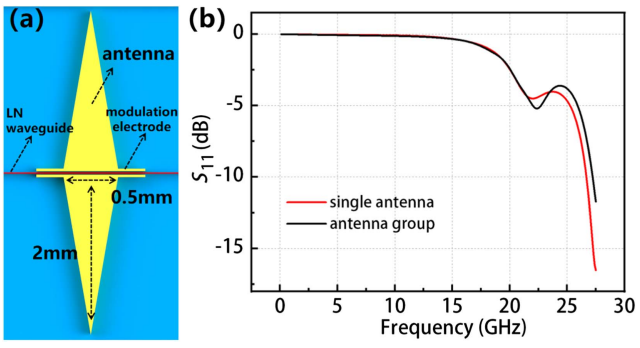

Fig. 1. (a) Schematic diagram of a conical dipole antenna. (b) S_{11} response of the antenna array.

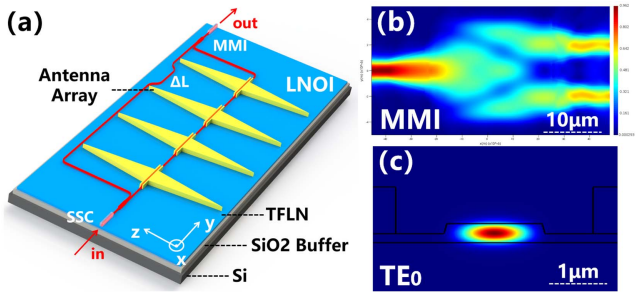

Fig. 2. (a) Schematic diagram of the electric field sensor structure. (b) Mode field distribution in the FDTD simulation MMI. (c) Mode field distribution in the waveguide in the modulation region.

the optical path difference designed for the two arms, which was set to be 54 μm, n denotes the effective refractive index of the waveguide, while λ signifies the input light wavelength. It can be seen from the formula that the linear working region of the device can be adjusted by changing the wavelength of the input light without the electric field. In the input and output parts, the waveguide width was set to be 1.1 μm, and the etching depth is 260 nm to ensure the single-mode condition for the 1.55 μm wavebands. In the modulation region, in order to reduce the additional scattering loss caused by the single-mode narrow waveguide, the waveguide width in the modulation region was extended to 1.8 μm through the adiabatic taper transition. Furthermore, the gap between the electrodes on either side of the waveguide is configured at 7 μm, thus minimizing potential metal absorption losses arising from electrodes being positioned too closely. Under these conditions, we conducted simulation-based optimization using FDTD software for the MMI structure and the wide-waveguide modulation region, as depicted in Figs. 2(b) and 2(c). The objective was to reduce losses across various sections of the electric field sensor while maintaining comparable performance.

3. Device Fabrication and Test

Given the requirement for the electric field direction within the modulation region to align with the Z-axis of the lithium niobate crystal, the device is fabricated on an X-cut LNOI platform, where the thickness of the thin-film lithium niobate layer is 500 nm, the thickness of the buried oxide layer below the lithium niobate is 4.7 μm, and beneath this oxide-doped layer, the silicon substrate is about 500 μm. Initially, we employed electron beam evaporation (EBE) to deposit a layer of Cr onto the surface of the lithium niobate, which served as a robust mask. Next, a layer of photoresist was spun onto the surface, followed by the utilization of electron beam lithography (EBL) to create a pattern on the photoresist. After exposure and development, inductively coupled plasma (ICP) etching was employed to conduct a two-step etching process, transferring the images onto the hard mask and the thin-film lithium niobate, respectively. The etch depth reached 260 nm. Finally, residual Cr on the surface was removed using a Cr etchant, resulting in the fabrication of the waveguide and MMI structure. Due to the utilization of a double-layer inverted taper structure in the spot size converter (SSC), the second-layer taper of the SSC needs to undergo repeated etching, following the same process as described above, in order to achieve the complete SSC structure. The electrode section involves an initial step of spin-coating a thicker layer of photoresist, followed by the employment of electron beam lithography (EBL) for pattern exposure. After development, electron beam evaporation (EBE) is used to deposit a metal layer onto the sample. In this case, we utilize Au as the material. Subsequently, the sample is immersed in an acetone solution for the lift-off process, resulting in the formation of the electrodes. Finally, a protective layer of silicon dioxide (SiO_2) is deposited onto the device surface using plasma-enhanced chemical vapor deposition (PECVD) to prevent contamination-related losses of the sample.

The microscope image of the sample after preparation is shown in Figs. 3(a)–3(c). The length of the device is about 7.5 mm, and the width is about 4.5 mm. After preparation, the optical loss of the multimode interference coupler (MMI) and the device was tested and evaluated by a tunable laser and an optical power meter. The test structure is shown in Fig. 4(a). Due to the relatively low losses of a single MMI device, the insertion loss for the 1.55-μm wavebands is obtained by measuring the average loss of six identical cascaded MMIs, as illustrated in Fig. 3(d). During the test, we obtained different transmission spectra by moving the output port from the 1st level to the 6th level, as shown in Fig. 4(b). After removing the grating losses, we calculated losses at each level and then calculated a relatively accurate insertion loss for a single MMI. This approach yielded an approximate loss of −0.35 dB for a single MMI device within the 1.55-μm waveband. Simultaneously, the laser wavelength was adjusted to scan the device's transmission spectrum, as demonstrated in Fig. 4(c). For a more intuitive representation of the on-chip losses of the device, we have subtracted the losses of two SSCs, where the SSC loss is approximately −1.5 dB/facet. It can be observed from the graph that the on-chip losses are approximately −3.7 dB, with an extinction ratio (ER) of >20 dB. Meanwhile we measured the bandwidth of the device, as shown in Fig. 4(d). The results were obtained using the rectangular coaxial transmission line (TEM cell) in the frequency range of 0.1 to 1 GHz, while the remaining results were measured in a microwave anechoic chamber.

Subsequently, the electric field sensor under evaluation is positioned within a standardized electric field for the measurement of the QAM signal, as depicted in Fig. 5. Upon signal generation by the QAM signal source, a standard electric field, operating at a frequency of 2 GHz, is induced within the TEM cell through the utilization of a high-power amplifier. Furthermore, the signal modulation rate is set to be 5 Mbaud/s. In the measurement setup, a microwave power meter is employed to monitor real-time power fluctuations of the signal source. During measurements, efforts are made to maintain the

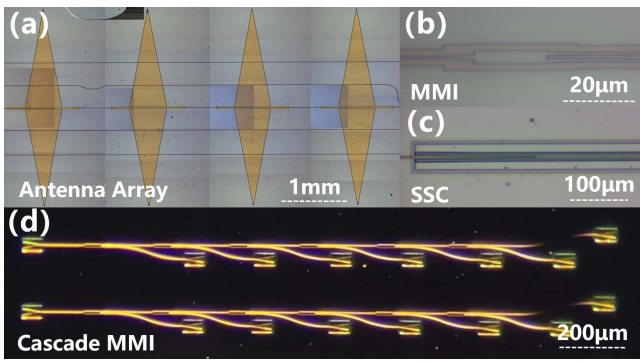

Fig. 3. (a) Microscope image of antenna array. (b) Microscope image of the 1 × 2 MMI. (c) Microscope image of the SSC. (d) Microscope image of the cascade MMI.

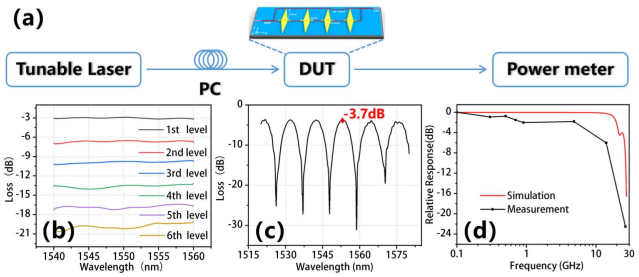

Fig. 4. (a) Schematic diagram of the device optical loss test structure. (b) Cascade 1 × 2 MMI optical loss test. (c) Transmission spectrum of the device. (d) Bandwidth of the device.

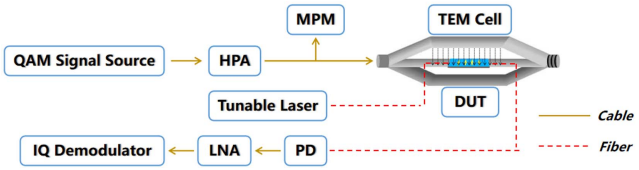

Fig. 5. Measurement setup for the electric field above 2 GHz. HPA, high-power amplifier; MPM, microwave power meter; PD, photodetector; LNA, low noise amplifier.

amplitude uncertainty of the standard electric field within ±1 dB. By carefully adjusting the output wavelength of the tunable laser, the sensor is optimally biased at its intersection, enhancing the dynamic range.

To calibrate the extra error brought by the experiment system, we connect the signal source and receiver directly without the sample, and the test results were collected as the standard data, as depicted by the red dots in Figs. 6(a)–6(c). These data would be compared with the data collected by the electric field sensor. Later, we measured the QAM signals by using the electric field sensor in the TEM cell, and the results were collected and are shown as blue dots in Figs. 6(a)–6(c). It could be observed from the figure that signals below 64-QAM exhibit a favorable distribution. The error vector magnitude (EVM) stands for the deviation between the experimental data and the standard data, which is consistently maintained below 8%. It also indicates that under these conditions, the system's bit-error-rate (BER) will remain at a relatively low level since the EVM is connected to the BER. Furthermore, as we progressively increase the carrier frequency from 2 GHz to 6 GHz under the condition of 16-QAM, an observable trend emerges: the signal's EVM gradually increases from 7.63% to 8.69%. This increase signifies a gradual degradation in signal transmission. Moreover, as we keep the carrier frequency at 2 GHz and then gradually change the signal modulation rate from 5 Mbaud/s to 10 Mbaud/s, the signal's EVM also experiences a gradual rise from 7.63% to 10.67%. The results are shown in Fig. 6(d). It could be observed that the modulation rate has a more significant influence on the EVM value than the changes in the carrier frequency.

In the aforementioned tests, it is evident that an increase in carrier frequency corresponds to a gradual increase in the error

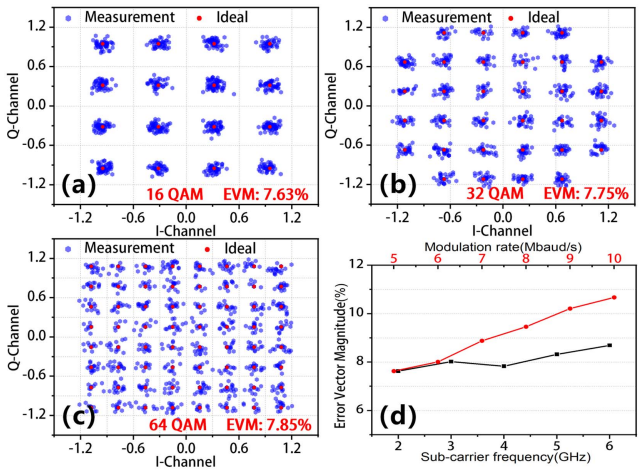

Fig. 6. (a) Test Images of the 16-QAM signals. (b) Test Images of the 32-QAM signals. (c) Test Images of the 64-QAM signals. (d) Error vector magnitude (EVM) variation trend with carrier frequency and modulation rate.

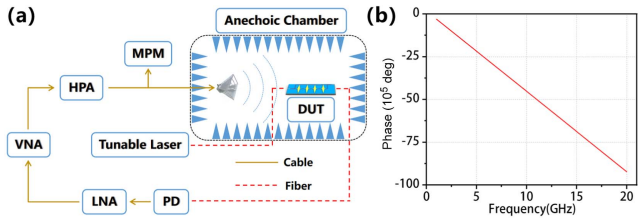

Fig. 7. (a) Measurement setup for the phase-frequency response test. VNA, vector network analyzer. (b) Phase-frequency response of the device.

vector magnitude (EVM) of the test signal. Beyond a frequency of 6 GHz, the EVM value becomes unacceptable. However, as indicated by the previous test results[27], the device's bandwidth exceeded 20 GHz. Consequently, for other frequencies, we investigate the device's delay processing by examining the phase-frequency response of the sample. The measurement configuration is depicted in Fig. 7(a). The entire testing environment is established in an anechoic chamber, with the horn antenna generating the electric field within the environment. This observation underscores the relatively favorable linearity of the sample signal within the frequency range of 1–20 GHz, as shown in Fig. 7(b), with consistent signal delays across different frequencies in this range.

4. Conclusion

In conclusion, we experimentally demonstrated an electric field sensor based on the TFLN platform. The measurement fiber-to-fiber loss is −6.7 dB, and the MZI structure exhibits an extinction ratio of greater than 20 dB. Moreover, we measured 16-QAM signals from 2 to 6 GHz, showing an EVM of less than 8%. Lastly, we measured the phase-frequency response of this device from 1 to 20 GHz.

In terms of optical losses, after subtracting two SSC port losses at −3 dB, two MMI losses at −0.7 dB, and a waveguide loss at −0.75 dB, it is evident that the residual loss is attributed to the tapered dipole antenna array at −2.25 dB. For signal measurement, we acquired 16-QAM, 32-QAM, and 64-QAM constellation diagrams of the sample at a modulation rate of 5 Mbaud/s and a carrier frequency of 2 GHz. These data were collected using the TEM cell. Furthermore, we plotted the EVM-frequency curve by increasing the carrier frequency from 2 to 6 GHz, while simultaneously collecting EVM values with an increased modulation rate from 5 Mbaud/s to 10 Mbaud/s. Despite the device having a bandwidth of over 20 GHz, the EVM value decreased rapidly when the carrier frequency exceeded 6 GHz during the measurement. From another perspective, we evaluated the sample's phase-frequency curve and observed a linear relationship within the 20 GHz range, which reveals good linear control of the device below 20 GHz.

The test results demonstrate that the reception performance of the QAM signals in the current sample is primarily limited by the increased frequency. We attribute this phenomenon to the device's signal-to-noise ratio (SNR), which we believe can be addressed by further enhancing the device antenna's design. Additionally, there is still room for improvement in optical loss, which could be addressed through optical design refinement, fabrication enhancement processes, and expansion of the electrode gap.

Overall, the QAM signal testing provides further evidence that the electric field sensor based on the thin-film lithium niobate Mach–Zehnder interferometer structure not only achieves a compact size, large bandwidth, and extensive dynamic range for measuring the electric field but also accurately recovers phase information from the complex electromagnetic environment. This achievement holds significant importance, especially in the face of increasingly intricate electromagnetic environments. Through continued device design optimization and fabrication enhancement, we are confident that electric field sensors based on the LNOI platform can be applied in an even wider array of complex environments.

Acknowledgement

This work was supported by the National Key Research and Development Program of China (No. 2021YFB2800104) and the National Natural Science Foundation of China (Nos. 62175079 and 62205119). We thank the Center of Micro-Fabrication and Characterization (CMFC) of WNLO and the Center for Nanoscale Characterization & Devices (CNCD), WNLO of HUST, for the facility support.

References

1. A. Nauman, Y. A. Qadri, M. Amjad, Y. B. Zikria, M. K. Afzal, and S. W. Kim, "Multimedia internet of things: a comprehensive survey," IEEE Access **8**, 8202 (2020).
2. D. C. Nguyen, M. Ding, P. N. Pathirana, A. Seneviratne, J. Li, D. Niyato, O. Dobre, and H. V. Poor, "6G internet of things: a comprehensive survey," IEEE Internet Things J. **9**, 359 (2022).
3. A. Mosaddeghi, D. Pavanello, F. Rachidi, M. Rubinstein, and P. Zweiacker, "Effect of nearby buildings on electromagnetic fields from lightning," J. Light. Res. **1**, 52 (2009).
4. A. Ebrahimi, J. Scott, and K. Ghorbani, "Ultrahigh-sensitivity microwave sensor for microfluidic complex permittivity measurement," IEEE Trans. Microw. Theory Tech. **67**, 4269 (2019).
5. Z. L. Wang, "Triboelectric nanogenerator (TENG)—sparking an energy and sensor revolution," Adv. Energy Mater. **10**, 2000137 (2020).
6. H. Wang, L. Zhou, Y. Liu, F. Liu, X. Liang, F. Liu, Y. Gao, X. Yan, and G. Lu, "UV-activated ultrasensitive and fast reversible ppb NO_2 sensing based on ZnO nanorod modified by constructing interfacial electric field with In_2O_3 Nanoparticles," Sens. Actuators B **305**, 127498 (2020).
7. H. Lv, Z. Yang, S. J. H. Ong, C. Wei, H. Liao, S. Xi, Y. Du, G. Ji, and Z. J. Xu, "A flexible microwave shield with tunable frequency transmission and electromagnetic compatibility," Adv. Funct. Mater. **29**, 1900163 (2019).
8. D. Baudry, C. Arcambal, A. Louis, B. Mazari, and P. Eudeline, "Applications of the near-field techniques in EMC investigations," IEEE Trans. Electromagn. Compat. **49**, 485 (2007).
9. D. Kumar, N. R. Prakash, and S. Singh, "Electric field sensor for electromagnetic pulse measurement," IETE Tech. Rev. **36**, 614 (2019).
10. A. Kainz, H. Steiner, J. Schalko, A. Jachimowicz, F. Kohl, M. Stifter, R. Beigelbeck, F. Keplinger, and W. Hortschitz, "Distortion-free measurement of electric field strength with a MEMS sensor," Nat. Electron. **1**, 68 (2018).
11. F. Yang, X. Fang, X. Chen, L. Zhu, F. Zhang, Z. Chen, and Y. Li, "Monolithic thin film lithium niobate electro-optic modulator with over 110 GHz bandwidth," Chin. Opt. Lett. **20**, 022502 (2022).
12. D. Zhu, L. Shao, M. Yu, R. Cheng, B. Desiatov, C. J. Xin, Y. Hu, J. Holzgrafe, S. Ghosh, A. Shams-Ansari, E. Puma, N. Sinclair, C. Reimer, M. Zhang, and M. Lončar, "Integrated photonics on thin-film lithium niobate," Adv. Opt. Photonics **13**, 242 (2021).
13. R. Wu, M. Wang, J. Xu, J. Qi, W. Chu, Z. Fang, J. Zhang, J. Zhou, L. Qiao, Z. Chai, and J. Lin, "Long low-loss-lithium niobate on insulator waveguides with sub-nanometer surface roughness," Nanomaterials **8**, 910 (2018).
14. M. Zhang, C. Wang, R. Cheng, A. Shams-Ansari, and M. Lončar, "Monolithic ultra-high-*Q* lithium niobate microring resonator," Optica **4**, 1536 (2017).
15. C. Wang, M. Zhang, X. Chen, M. Bertrand, A. Shams-Ansari, S. Chandrasekhar, P. Winzer, and M. Lončar, "Integrated lithium niobate electro-optic modulators operating at CMOS-compatible voltages," Nature **562**, 101 (2018).
16. X. Ma, X. Liu, C. Zhuang, and R. Zheng, "High sensitivity thin-film lithium niobate electric field sensor," in *IEEE International Conference on High Voltage Engineering and Applications (ICHVE)* (2022), p. 1.
17. Y. Xue, Z. Ruan, and L. Liu, "Electrode-free photonic electric field sensor on thin film lithium niobate with high sensitivity," Opt. Lett. **47**, 2097 (2022).
18. Y. Tian, S. Xie, S. Luan, Z. Guo, S. Zhang, and Y. Yang, "Broadband high-sensitivity thin-film $LiNbO_3$ based E-field sensor with LF-shaped electrode," IEEE Electron Device Lett. **44**, 1555 (2023).
19. G. S. Kanter, P. M. Moraw, K. F. Lee, F. A. Juneghani, M. G. Vazimali, K. Kim, N. K. Fontaine, and S. Fathpour, "Microwave electromagnetic field sensor on thin-film lithium niobate using photonic down-conversion detection," IEEE Photonics J. **15**, 5501406 (2023).
20. F. T. Sheehy, W. B. Bridges, and J. H. Schaffner, "60 GHz and 94 GHz antenna-coupled $LiNbO_3$ electro-optic modulators," IEEE Photon. Technol. Lett. **5**, 307 (1993).
21. W. B. Bridges, F. T. Sheehy, and J. H. Schaffner, "Wave-coupled $LiNbO_3$ electro-optic modulator for microwave and millimeter-wave modulation," IEEE Photon. Technol. Lett. **3**, 133 (1991).
22. S. Shinada, T. Kawanishi, T. Sakamoto, M. Andachi, K. Nishikawa, S. Kurokawa, and M. Izutsu, "A 10-GHz resonant-type $LiNbO_3$ optical modulator array," IEEE Photon. Technol. Lett. **19**, 735 (2007).

23. H. Murata, R. Miyanaka, and Y. Okamura, "Wireless space-division-multiplexed signal discrimination device using electro-optic modulator with antenna-coupled electrodes and polarization-reversed structures," Int. J. Microw. Wireless Technol. **4**, 399 (2012).
24. N. Kohmu, H. Murata, and Y. Okamura, "Electro-optic modulators using double antenna-coupled electrodes for radio-over-fiber systems," IEICE Trans. Electron. **E96-C**, 204 (2013).
25. H. Murata and Y. Matsukawa, "Millimeter-wave band optical single-sideband modulator utilizing antenna-coupled electrode with polarization-reversed structures and asymmetric Mach-Zehnder waveguide," in *International Topical Meeting on Microwave Photonics (MWP)* (2018), p. 191.
26. H. Murata, H. Yokohashi, S. Matsukawa, M. Sato, M. Onizawa, and S. Kurokawa, "Antenna-coupled electrode electro-optic modulator for 5G mobile applications," IEEE J. Microw. **1**, 902 (2021).
27. Z. Liu, H. Wu, W. Du, L. Zhao, M. Wang, B. Sun, Z. Zhang, S. Zhang, and Y. Liu, "Broadband electric field sensor with large dynamic range and high sensitivity based on lithium niobate on insulator," IEEE Photon. Technol. Lett. **35**, 1323 (2022).
28. M. Kanda and L. D. Driver, "An isotropic electric-field probe with tapered resistive dipoles for broad-band use, 100 kHz to 18 GHz," IEEE Trans. Microw. Theory Tech. **35**, 124 (1987).